

Neuromorphic information processing using ultrafast heat dynamics and quench switching of an antiferromagnet

J. Zubáč*^{†1,2}, M. Surýnek^{†2}, K. Olejník¹, A. Farkaš^{1,2}, F. Krizek¹, L. Nádvorník², P. Kubaščík², Z. Kašpar^{1,2}, F. Trojánek², R. P. Campion³, V. Novák¹, P. Němec², and T. Jungwirth^{1,3}

¹Institute of Physics of the Czech Academy of Sciences, Prague, Czech Republic

²Faculty of Mathematics and Physics, Charles University, Prague, Czech Republic

³School of Physics and Astronomy, University of Nottingham, United Kingdom

Abstract

Solving complex tasks in a modern information-driven society requires novel materials and concepts for energy-efficient hardware. Antiferromagnets offer a promising platform for seeking such approaches due to their exceptional features: low power consumption and possible high integration density are desirable for information storage and processing or applications in unconventional computing. Among antiferromagnets, CuMnAs stands out for atomic-level scalable magnetic textures, analogue multilevel storage capability, and the magnetic state's control by a single electrical or femtosecond laser pulse. Using a pair of excitation laser pulses, this work examines synaptic and neuronal functionalities of CuMnAs for information processing, readily incorporating two principles of distinct characteristic timescales. Laser-induced transient heat dynamics at sub-nanosecond times represents the short-term memory and causes resistance switching due to quenching into a magnetically fragmented state. This quench switching, detectable electrically from ultrashort times to hours after writing, reminisces the long-term memory. The versatility of the principles' combination is demonstrated by operations commonly used in neural networks. Temporal latency coding, fundamental to spiking neural networks, is utilized to encode data from a grayscale image into sub-nanosecond pulse delays. Applying input laser pulses with distinct amplitudes then allows for pulse-pattern recognition. The results open pathways for designing novel computing architectures.

1 Introduction

Recent breakthroughs in artificial intelligence and computing are revolutionizing diverse industries and our daily lives, driving further research in numerous areas of science and technology. Artificial neural networks are routinely used to solve sophisticated problems ranging from large datasets processing and decision-making over language understanding and text generation to object detection, image classification and pattern recognition. These networks were initially developed as mathematical abstraction of biological neural networks and, similarly to them, are comprised of nodes called neurons. However, artificial neurons retain only some fundamental characteristics of their biological counterparts. They possess adjustable synaptic weights and process information by performing the weighted summation of real-valued analogue inputs. The resulting sum is passed

*Email: zubac@fzu.cz

[†]These authors contributed equally.

to a thresholding nonlinear activation function, which is essential for the network to approximate a general nonlinear function [1]. In contrast with biological neurons, simplified artificial neurons are static, lacking any inherent temporal dynamics.

A somewhat different approach from that used in artificial neural networks is employed in spiking neural networks. These networks enable event-driven information processing and dynamic time-dependent calculations resembling neuro-biological systems called neuromorphic computing. The building blocks of spiking neural networks are spiking neurons, with a leaky-integrate-and-fire neuron model as a notable example. Like artificial neurons, spiking neurons integrate the weighted inputs and produce an output above a threshold. However, the weights are updated through the biologically inspired learning rule called spike-timing-dependent plasticity [2]. Instead of working with real-valued numbers, spiking neurons use the relative timing of short pulses called spikes. Similarly, as the photoreceptors in an eye convert the incoming light into trains of spikes with a frequency corresponding to light intensity, a bright pixel of a digital image can be represented by higher spiking rates than a darker one. This representation of inputs is called rate encoding [3]. Another timing-based encoding mechanism is termed temporal latency coding. The mechanism exploits the delay between individual spikes rather than their frequency. The encoding takes advantage of sparsely distributed spikes, i. e. only two spikes are, in principle, needed to encode a single data point. Benefiting from spike sparsity, it is particularly convenient for efficient data representation.

For practical employment of these biologically inspired concepts in computing, specifics of particular implementations have to be considered. Artificial neural networks, used for solving difficult problems of artificial intelligence, owed their success to the increasing computational performance of traditional computers. [4]. However, increasing energy costs and adverse environmental impacts when solving gradually more complex tasks [5, 6] question the efficiency of traditional hardware, which lags behind that of biological systems by orders of magnitude [1]. The efficiency gap is caused, i.a., by the hardware architectures internally working with digital signals, which are inconvenient for bio-inspired asynchronous operation, large data throughputs or analogue computations. Therefore, a dedicated hardware will be used for neuro-inspired computing in the future. This will involve transferring certain high-level functions of traditional chips to physical systems and devices using their intrinsic characteristics such as temporal dynamics, mutual interactions, multi-state stability or memory [7, 8]. Various memristive [9], optical [10] or magnetic systems [11] have been proposed to implement unconventional computing schemes such as reservoir computing or functions of synapses, neurons and whole networks. As for magnetic systems, this includes e. g. magnetic tunnel junctions [12, 13, 14] and spintronic oscillators [15, 16, 17], complex magnetic textures as skyrmions [18, 19, 20] or chiral magnets and domain walls [21, 22], magnetic heterostructures [23], compensated magnets [24, 25], magnons [26] or magnetic metamaterials such as artificial spin ices [27, 28, 29] or nanorings [30]. Applications of these spin-based systems range from using AFM/FM spin-orbit devices used as weights [31] for associative memory operation, over magnetic tunnel junctions employed as synapses and neurons for classification tasks [32, 33] to implementing reservoir computing schemes with magnons for pattern recognition [26].

Here, we explore the potential of an antiferromagnetic metal, CuMnAs, for unconventional computing applications. In previous works, magnetic properties [34, 35, 36] of CuMnAs films have been investigated including possible means of affecting the material's magnetic state [37, 38, 39, 40]. It was found, that the sample can be brought to a metastable high-resistive state by transient heating to the vicinity of Néel temperature (~ 480 K) using an μ s- to ns-scale electrical or fs-scale optical pulse [41]. This effect, called quench switching, can be characterized by room-temperature dynamics at milliseconds and seconds. Magnetic textures in CuMnAs and their control have been studied by microscopy methods [42, 36, 43] and the atomically sharp 180° domain walls were identified as a possible microscopical origin of the high resistance signals [44]. Works employing laser techniques have explored heat dissipation in CuMnAs layers at ultrashort timescales depending on their thickness [45] and showed how to separate the transient heat contribution from the non-linear quench switching and presented a phenomenological heat dissipation model [46].

In the present manuscript, we connect the short-term ultrafast sub-nanosecond heat dissipation phenomena, previously studied by advanced optical methods, with the quench switching, repre-

senting the long-term high-resistance memory to showcase neuromorphic information processing tasks. First, in Fig.1, we present the phenomenology of the quench switching, combining a pair of excitation femtosecond laser pulses and electrical readout down to nanosecond time resolution to elucidate physical principles and neuromorphic functions provided by CuMnAs. Second, in Fig.2, we process a grayscale image by temporal latency coding, encoding information from pixels into sub-ns delays between femtosecond laser pulses. Next, we employ unequal laser pulses for pattern recognition and propose applying the same principle for convolutional edge detection. Finally, we discuss the scalability needed for energy-efficient information processing and compare the antiferromagnetic CuMnAs with relevant magnetic and photonic systems used for solving similar neuromorphic tasks.

2 Results

In Fig. 1, we present neuronal and synaptic functions in an antiferromagnet, employing switching by optical stimuli and electrical readout. Experimentally, we excite the CuMnAs device prepared from a 20-nm-thick epilayer with two time-delayed 150-fs laser pulses, causing transient heating of the sample and recording its resistance with a high-frequency oscilloscope (Fig. 1a). By varying the input parameters of the experiment - pulse fluences and their mutual delay - we control the ultrafast temperature evolution at nanosecond and sub-nanosecond timescales and thus determine the strength of the quench switching effect. This is reflected in the resulting resistance, which comprises time-varying heat contribution linear in fluence, ΔR_{heat} , and the non-linear quench switching contribution, ΔR_{sw} , characterized by onset above the threshold fluence, F_{th} , and millisecond dynamics (insets of Fig. 1a). The arrangement corresponds to an artificial neuron, which integrates two weighted inputs in time and produces an output above a threshold (Fig. 1b, see also Supplementary Fig. S1 for functionalities provided by the CuMnAs device). In Figs. 1c, d we experimentally explore the thresholding at nanosecond times by changing the pulse delay. The resistance data are shown for identical laser pulses delayed by 4 ns and 10 ps, with the fluences $A_1 = A_2 = 17.1 \text{ mJ/cm}^2$. The fluence value is selected to ensure that none of the pulses reaches the switching threshold individually ($A_i < F_{\text{th}} \approx 22.2 \text{ mJ/cm}^2$), while the sum of pulse fluences exceeds the switching threshold ($A_1 + A_2 > F_{\text{th}}$). Due to the ultrafast heat dissipation on the order of $\sim 100 \text{ ps}$, most of the heat imposed by the first pulse is already removed from the sample when the second pulse impacts 4 ns later. Consequently, the sample is not heated above the critical threshold value, and no switching is observed (Fig. 1c). As the delay between pulses is reduced close to the characteristic heat dissipation time or below, the heat contributions from the two pulses add up and accumulated heat surpasses the critical threshold value, resulting in a noticeable switching signal ΔR_{sw} (Fig. 1d for $\Delta t = 10 \text{ ps}$). The ability of heat accumulation combined with the exponential decay in time due to dissipation is analogous to the leaky integration in the leaky-integrate-and-fire neuron model. To distinguish the signal ΔR_{sw} (insets of Figs. 1c, d) from ΔR_{heat} at the nanosecond times, where the two contributions overlap, we estimated the transient heat contribution by the sum of traces for individual sub-threshold pulses ($R_1 + R_2$), which we subtracted from the trace for both pulses applied simultaneously (R_{12}), i. e. $\Delta R_{\text{sw}} = R_{12} - \Delta R_{\text{heat}} \approx R_{12} - (R_1 + R_2)$. At times after impact longer than $\approx \mu\text{s}$, the heat has already been fully dissipated from the sample to the substrate and only the switching signal ΔR_{sw} adds up to R_0 . Hence, the amplitude of the switching signal can be evaluated directly from the traces measured over a 10-ms window by fitting to the stretched exponential function $\sim \exp((-t/\tau)^\beta)$ for $t \gtrsim \mu\text{s}$ with $\tau = 4 \text{ ms}$. In this way, information about sub-nanosecond pulse delays can be retrieved at milliseconds, providing temporal scalability across several orders of magnitude without the necessity of implementing ultrafast readout. This approach can be conveniently employed for representing and processing data, as we will show further.

Beside changing delay between pulses, we can also control the heat accumulation and switching by adjusting their fluences. The fluence-dependent resistance traces in the 10-ms window range for a constant pulse delay $\Delta t = 10 \text{ ps}$ are presented in Fig. 1e. Whereas the resistance trace for 19 mJ/cm^2 is dominated by heat contribution, approaches R_0 after the heat fades away and shows

no switching signal, the other traces exhibit the switching manifested by increased resistance at microsecond and millisecond times. Fig. 1f then summarizes previous figures by displaying the switching signal ΔR_{sw} for various fluences as a function of the pulse delay Δt . It has been shown that the observed dependence can be explained by the heat dissipation model comprising several contributions of various origins [46]. The variation at ~ 100 -ps timescales can be attributed to ultrafast heat dissipation mediated by phonons. Although the heat dissipation time constant typical for the 20-nm CuMnAs film is ~ 500 ps [45], ΔR_{sw} varies more rapidly than that (~ 200 ps), further enhancing the temporal resolution provided by the switching signal. The distinction is the consequence of the ΔR_{sw} dependence on fluence, which is, in contrast with ΔR_{heat} , non-linear, as highlighted by the experimental data in the inset of Fig. 1f.

Combining the ultrafast heat dynamics triggered by time-delayed femtosecond laser pulses and the antiferromagnetic memory opens up pathways for sub-nanosecond information processing, as presented in Fig. 2. The technique used is called temporal latency coding: We encode the information from a greyscale image (Fig. 2a) into mutual time delays of two equal pulses (Fig. 2b). Using the previously acquired experimental ΔR_{sw} vs Δt dependence (Fig. 2e), the image of dimensions 28×28 pixels is converted into delays in such a way that the image's 256 levels of grey are linearly mapped onto the range of ΔR_{sw} . The appropriate delay Δt is then obtained from ΔR_{sw} as the inverse function. This procedure led in our setting to delays from 10 to 2000 ps. Next, we perform the two-pulse switching experiment sequentially using these delays as inputs. From the measured resistance traces, we evaluate the map of switching signal ΔR_{sw} as presented in Fig. 2c. The resulting ΔR_{sw} map reproduces the original image (Fig. 2a) and captures the information from the sub-ns delay map (Fig. 2b), but it has an opposite contrast, i.e., shorter delays lead to a larger signal. Contrary to the ultrafast pulse delays, the information in the switching signal can be retrieved at microseconds and milliseconds after the pulses' impact using a conventional electrical readout.

In Fig. 2d, we study the reliability of the used encoding procedure by recognizing different pulse delays from the switching signal, ΔR_{sw} . We selected four different delays from 0 to ~ 3000 ps using the experimental data from Fig. 1f for fluences showing a non-zero switching signal in the pulse overlap. The signal was always normalized to a value of maximal signal reached for short pulse delays and fitted to a Gaussian function. The underlying data distributions had standard deviations from 0.10 to 0.12 of normalized ΔR_{sw} , illustrating the possible discernible states and the noise of the data that determine the maximum information transfer rate (see Shannon-Hartley theorem, e.g. in Ref. [47]). Figs. 2f-i show the relation between the heat and switching signal contributions to the resistance and following signal fading by comparing the resistance traces at different laboratory times. Whereas short after the pulses' impact, the resistance variation ΔR is dominated by the heat contribution (see Fig. 2f for $t = 12$ ns), the remaining Figs. 2g-i at millisecond times show solely the switching signal. By comparing Fig. 2f and Fig. 2g, it is apparent that the information from the heat is translated into the switching signal. Additionally, Figs. 2g-i show the signal variation at μs and ms times. The illustrated signal decline and its vanishing, given by the memory's metastability and switching signal dynamics, are crucial for time-division multiplexing - the capability to reuse the device again after the memory's forgetting period without the necessity of resetting the system's magnetic state by field or thermal cycles. The switching signal fading memory and the information transfer across orders of magnitude in time due to the combination of the short-term heat-related memory and the long-term switching-signal memory are remarkable features demonstrating the system's information encoding capabilities.

Next, in Fig. 3, we show that our system can be used not only for the information encoding into delays but also for recognizing patterns of pulses at ultrashort times when distinct pulse amplitudes are employed. Fig. 3a shows the sub-ns delay dependence of the switching signal ΔR_{sw} for two pulses of different fluence ratios but the same sum of fluences. Here, the pulse fluences are again selected to lie below the switching threshold individually but exceed the threshold in total. In contrast with the reference equal-pulse case symmetric with respect to Δt to $-\Delta t$ conversion (red curve), the switching signal for a given pulse delay is larger when the weaker pulse is followed by a stronger (green curve and $\Delta t > 0$, blue curve and $\Delta t < 0$) and lower when the stronger pulse is followed by a weaker one (green curve and $\Delta t < 0$, blue curve and $\Delta t > 0$). The manifested

behaviour can be understood considering the ultrafast heat dissipation in the material. The temperature evolution after the impact of the pulses can be approximated [46] as

$$\Delta T(t) \approx A_1 \exp^+\left(-\frac{t}{\tau_{\text{ph}}}\right) + A_2 \exp^+\left(-\frac{t - \Delta t}{\tau_{\text{ph}}}\right), \quad (1)$$

where A_1 and A_2 are the pulse amplitudes, $\tau_{\text{ph}} \sim 500$ ps is the heat dissipation time and $\exp^+(-x) = \exp(-x)\Theta(x)$ is the exponential function multiplied by the Heaviside step function $\Theta(x)$. Since the amount of the dissipated heat scales with the pulse amplitude, the temperature generally reaches a different value at $t = \Delta t$ for the opposite order of the pulses. In our setting, where the ratios of pulse amplitudes A_1 and A_2 are $\frac{1}{2}, \frac{2}{1}$ or $\frac{1}{1}$ and their sum is $A_1 + A_2 \approx 1.48 F_{\text{th}}$, it leads to a different maximal temperature reached after the impact of the second pulse (see the inset of Fig. 3a). This difference is translated into different values of the switching signal being recorded at ms-times since its amplitude is a function of the maximal temperature, with a non-linear onset at F_{th} . Additional discussion of the heat dissipation and the switching behaviour is provided in Section 2 of the Supplementary material. In Fig. 3c, we present the respective experimental resistance traces for the three fluence ratios recorded in the 10-ms window and the selected pulse delay $\Delta t = 142$ ps. The curves further demonstrate switching signals dependence on the distribution of the total fluence into fluences of individual pulses. It shows that the switching signal is larger for a sequence $A_1 A_2$ of a small pulse followed by a larger one than for the opposite pulse order. The accuracy of recognizing pulse patterns consisting of two pulses with amplitudes A_1 and A_2 , can be as high as $\sim 98\%$ as we corroborate in supplementary Fig. S3 using all four combinations of A_1 and A_2 and $\Delta t = 150$ ps. The presented recognition of patterns using two pulses can be further used as a basis for more subtle processing, e.g., it can be extended into a case of multiple pulses representing additional inputs, or it can be used to perform more complex operations. In supplementary Fig. S4, we propose the application of pulse-order recognition for convolutional edge detection using a binary image as the input data. Finally, we discuss the prospects of the antiferromagnetic CuMnAs material for designing novel computing architectures by studying devices' lateral and vertical scalability and energy efficiency. Fig. 4a shows the relative single-pulse switching signal $\Delta R_{\text{sw}}/R_0$ plotted against the energy of the laser pulse incident onto the samples' active region for devices of various sizes. The devices were prepared from the 20-nm-thick CuMnAs film, and the dimensions of their active region were approximately $w \times 2w \mu\text{m}^2$, where w is the device width. The full width at half maximum of the incident laser beam was 20 μm , always safely covering the entire active region. As the dimensions are scaled from the 10- μm -wide bar down to sub-1- μm^2 device, the amount of energy impacting the device needed to reach the switching signal $\Delta R_{\text{sw}}/R_0 = 0.2\%$ drops from ~ 10 nJ to sub-0.1-nJ values. Despite scaling, the multilevel character of the switching and temporal relaxation of the signal is preserved, indicating that the magnetic textures in CuMnAs responsible for the quench switching signals are much smaller than the size of the smallest prepared device, i.e. $0.5 \mu\text{m}^2$. Indeed, the previous microscopy study based on DPC-STEM and micromagnetic XMLD-PEEM imaging [44] revealed a potential source of the quench switching signal in spin textures and sharp domain walls at the atomic scale, well below the detection limit of the XMLD-PEEM method (~ 10 nm). Extrapolating the nearly linear dependence of threshold energy on the device size (inset of Fig. 4a) down to $\sim 10 \times 10 = 100$ nm² dimensions leads to an energy estimate of ~ 10 fJ for such a minuscule, yet still conceivable device. The value of ~ 10 fJ needed for switching lies beyond the current limits of the energy cost per floating point operation in modern CMOS microprocessors (~ 150 fJ, [48]), is commensurate with the most energy-efficient magnetic memories used for neuromorphic computing ($\lesssim 100$ fJ [49, 50, 2]) or state-of-the-art organic artificial synapses [51], and comparable with characteristic energy per synaptic event in biological systems ($\sim 1 - 100$ fJ, [52]). Further improvement of energy efficiency and heat dissipation properties of devices can be achieved by scaling the vertical dimensions of layers and reducing their thickness. Fig. 4b compares the delay dependence of ΔR_{sw} , given by the heat dissipation, in the 50-nm and 20-nm CuMnAs film. Whereas in the thicker sample, the thermal relaxation takes more than 1 ns, the heat in the 20-nm sample is dissipated within ~ 500 ps. The previous report [45] consistently demonstrated heat dissipation times approximately proportional with the layer thickness, with values $\lesssim 100$ ps for the

thinnest, less than 10 nm thick, layers. Moreover, decreased film thickness improves heat transfer efficiency not only through the reduction of heat dissipation times but also by limiting the relative amount of residual heat accumulated in the sample [46], enabling possible denser integration of devices and increasing their endurance by mitigating thermal degradation.

3 Discussion

In this article, we explored synaptic and neuronal functionalities of the antiferromagnetic CuMnAs device for scalable and energy-efficient information processing using the electrical readout and a pair of femtosecond laser pulses as the input stimulus. We demonstrated the encoding of a grayscale image by temporal latency coding, transferring information from sub-ns delays to switching signal at milliseconds (Fig. 2). We also showed how to use the combination of ultrafast heat dynamics and quench switching of an antiferromagnet for recognizing pulse patterns at ~ 100 ps timescales (Fig. 3) and proposed utilization in convolutional edge detection (Supplementary Fig. S4). Let us now review several physical systems and devices exploiting related techniques and principles which were used to address similar tasks and compare them with the results of this article.

We start with the observation from Fig. 4 that both the $10\mu\text{m}$ -wide CuMnAs device and a much smaller, sub- $1\text{-}\mu\text{m}^2$ device exhibit the same multilevel field-insensitive switching characteristics due to expected atomic-level sizes of the underlying magnetic textures, highlighting devices' ultimate scalability. Previous works employing compensated magnets for neuromorphic applications relied on features of micrometer-sized domains with implications for the functionalities. In Ref. [23] studying neuronal functions realized by spin-orbit torque switching in the antiferromagnet/ferromagnet heterostructure, the multistability was attributed to an intermediate state due to local exchange bias variations at ~ 200 nm scales leading to a transition from multistable switching for the $5\text{-}\mu\text{m}$ device to probabilistic binary switching for the device smaller than $1\text{ }\mu\text{m}$. Moreover, the magnetic field was required for reinitiation of the device's magnetic state and its repeated use. The article [25] presented synaptic behaviour for ultrafast neuromorphic computing in the compensated ferrimagnet switched under magnetic field by spin-orbit torques. Gradual changes of synaptic weights were realized by electrical switching with 10-ns pulses and ~ 30 pulses were needed for the full magnetization reversal. Both works used electrical pulses with ≥ 1 ns duration, which limits the temporal resolution for switching by the coincidence of two pulses. On the contrary, the method presented in this article provided a resolution at ~ 100 -ps times permitted by the ultrafast heat dissipation in CuMnAs layers (Figs. 1f and 4b).

As for applications of physical systems for solving tasks, pattern recognition based on non-linear scattering of magnons was demonstrated in a magnonic Ni-Fe reservoir excited in the high-power regime at GHz frequencies [26]. Two microwave pulses of distinct frequencies with the 20-ns envelope were used as the excitation, and Brillouin light spectroscopy was used as the readout. The maximal difference between the spectra corresponding to the opposite pulse order, connected to the highest pattern recognition efficiency, was recorded in the case of partially overlapped pulses with $\Delta t \sim 10$ ns. Furthermore, in Ref. [53] authors presented ultrafast photonic neuromorphic image processing using a single neuron represented by a commercially available vertical cavity surface emitting laser (VCSEL). Similarly to our approach, the authors take advantage of the temporal integration of laser pulses, causing the production of neuron output above a threshold, which is, in their case, reached only when all the input pulses have the same negative polarity. The method was applied for convolutional edge detection with 2×2 kernels using 3-ns delays between input laser pulses, consuming 1.2 pJ per operation. In this work, analogous functionalities such as in Refs. [26, 53] has been realized by the new method based on quench switching in an antiferromagnet, with competitive energy efficiency and shorter temporal pulse separation (~ 100 ps). Moreover, both excitation and readout can be performed optically as well as electrically in our system (Ref. [41] and Supplementary Fig. S6), further highlighting the versatility by enabling all-optical operation with free-space connectivity on the one hand, and more accessible all-electrical operation on the other. The recent work [54] also confirmed the same switching effect as in CuMnAs in a different, higher Néel temperature antiferromagnet, allowing for enhancing device properties

for neuromorphic computing through material optimization.

4 Conclusion

In summary, we studied a novel concept for neuromorphic information processing using an antiferromagnet, combining the short-term ultrafast heat dynamics and the long-term quench switching. The two phenomena of distinct dynamics can be used for temporal latency encoding, inherent information representation in spiking neural networks. Recognition of patterns, achieved at ~ 100 ps by employing pulses of different amplitudes, is then an essential operation for various data processing tasks, with applications in computer vision or signal analysis. Experimental realization of these functions at ultrashort times paves the way for efficient time-multiplexed in-materia computing using compensated magnets.

5 Experimental Section

5.1 Sample preparation and device fabrication

Thin films of tetragonal CuMnAs with 20 and 50 nm thickness were grown by molecular epitaxy on GaP(001) substrate. Simple two-terminal bars used for experiments were prepared by electron beam lithography and wet etching. Then, we used the evaporation technique to equip the bars with golden contacting pads, assuring similar resistance of devices from the same batch, independently on exact contact positioning. Further details about the thin film characterization can be found in Ref. [55].

5.2 Optical measurements

The optical experiments were performed using a femtosecond laser system Pharos by Light Conversion. The laser pulse duration was 150 fs and the central wavelength was 1030 nm. A sketch of the experimental setup can be found in the Supplementary material (Fig. S4). Details about the experimental setup can be found in Ref. [46].

5.3 Electrical measurements

Time-resolved electrical measurements were performed using a Rohde & Schwarz RTP064 high-performance oscilloscope with 6 GHz bandwidth for readout and Rigol DG1000Z as a voltage source. We recorded the voltage U of the input resistance of the oscilloscope connected in series with the sample and calculated the sample's resistance.

We typically collected 2.5M points over a 10 μ s or a 10 ms window during one acquisition, which was started by receiving a timing reference signal from the laser. To reduce the noise at high frequencies without losing the time resolution, we acquired the data in a stroboscopic regime with a 100-Hz laser duty cycle and averaged out curves from ~ 100 acquisitions. Schematics of the experimental setup can be found in the Supplementary material (Fig. S4).

Supporting Information

Supporting Information is available from the Wiley Online Library or from the author.

Acknowledgements

T.J. acknowledges Ministry of Education of the Czech Republic Grant No. CZ.02.01.01/00/22008/0004594 and LM2023051 and ERC Advanced Grant No. 101095925. J.Z., K.O., A.F., F.K., and Z.K. acknowledge support from Czech Science Foundation Grant No. 21-28876J.

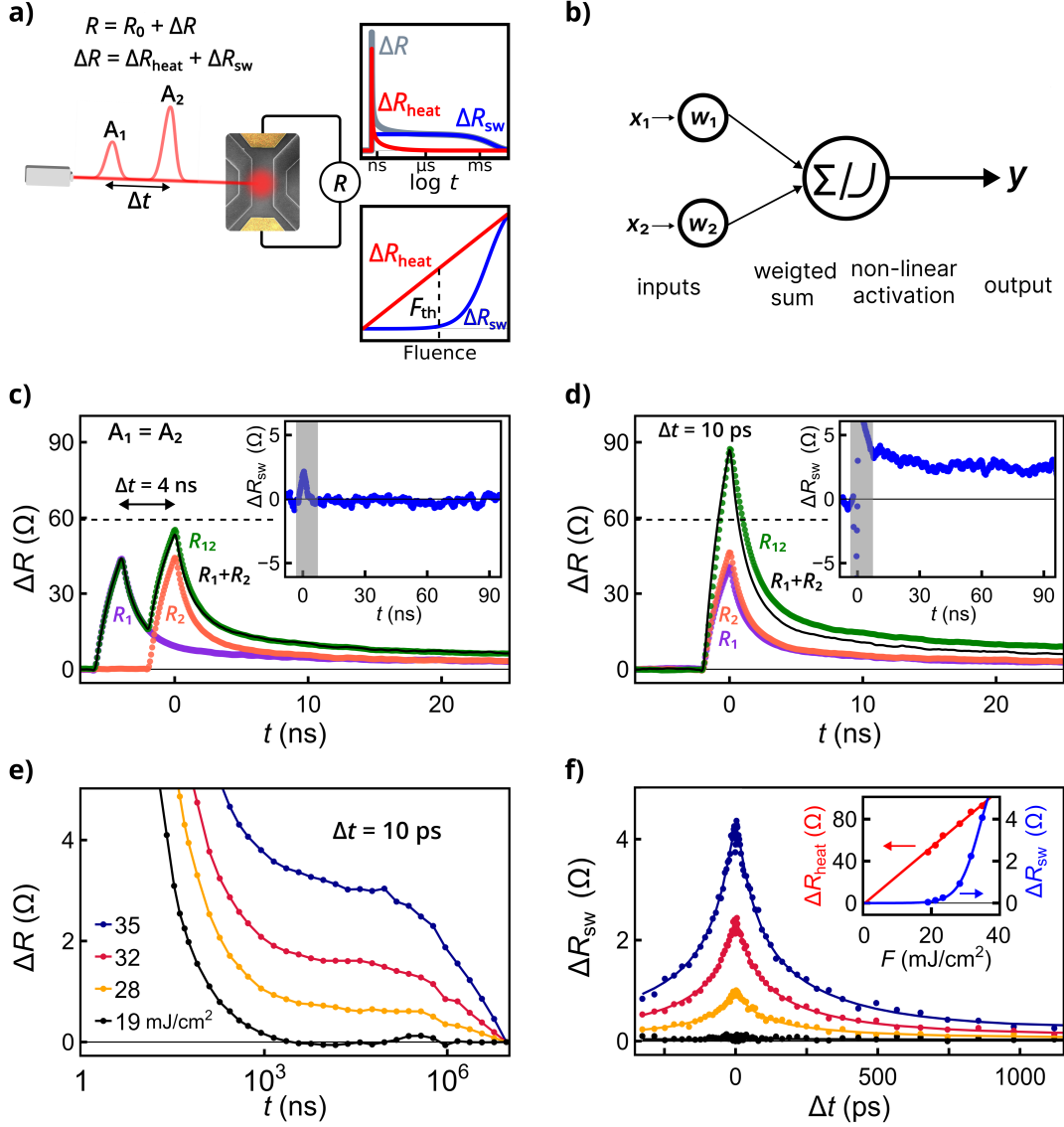


Figure 1: Neuronal and synaptic functionalities realized in an antiferromagnet by optical switching using two laser pulses. (a) Design of the experiment: A 10- μm wide CuMnAs bar device prepared from a 20-nm epilayer is excited by two 150-fs input laser pulses of variable fluences delayed by Δt . The full width at half maximum of the incident Gaussian beam is 20 μm . A high-performance oscilloscope with $\sim\text{ns}$ resolution was used to obtain the resulting longitudinal resistance R . The resistance R consists of resistance offset R_0 and time-varying part ΔR_{sw} , comprising switching-signal (ΔR_{sw}) and heat (ΔR_{heat}) contributions (upper inset panel). ΔR_{heat} and ΔR_{sw} are fluence dependent (lower inset panel) with a characteristic onset in ΔR_{sw} above switching fluence threshold F_{th} . (b) An artificial neuron taking two inputs. The neuron integrates weighted inputs x_1 and x_2 and produces an output once the weighted sum surpasses the threshold of an activation function. In the case of a dynamic neuron, integration is done over time and with a leakage. (c) Resistance evolution at ns-timescale after the impact of two identical pulses delayed by 4 ns (green) and the same pulses applied individually (orange, purple). The black line is the ordinary sum of the orange and purple traces. Inset shows a resistance signal obtained by subtracting the sum from the experimental curve for both pulses. The grey area marks the region where the signal ΔR_{sw} is ambiguous due to the uncertainty of the measurement method. The total fluence of the two pulses was 34.3 mJ/cm^2 . (d) Same as in (c) for the delay $\Delta t = 10$ ps. The non-zero signal ΔR_{sw} (inset) appears after the resistance reaches the threshold for switching (dashed line). (e) Resistance evolution after the impact of two identical pulses delayed by $\Delta t = 10$ ps measured over the temporal range of 10 ms. A detail of the resistance part with prevailing switching contribution is shown for several cumulative fluences. (f) Switching signal ΔR_{sw} as a function of Δt for a pair of pulses and same fluences as in (e). Inset shows the experimental dependence of ΔR_{heat} and ΔR_{sw} on the total fluence. The solid line is a fit of ΔR_{heat} to a linear function, respectively a fit of ΔR_{sw} to a sigmoid activation function.

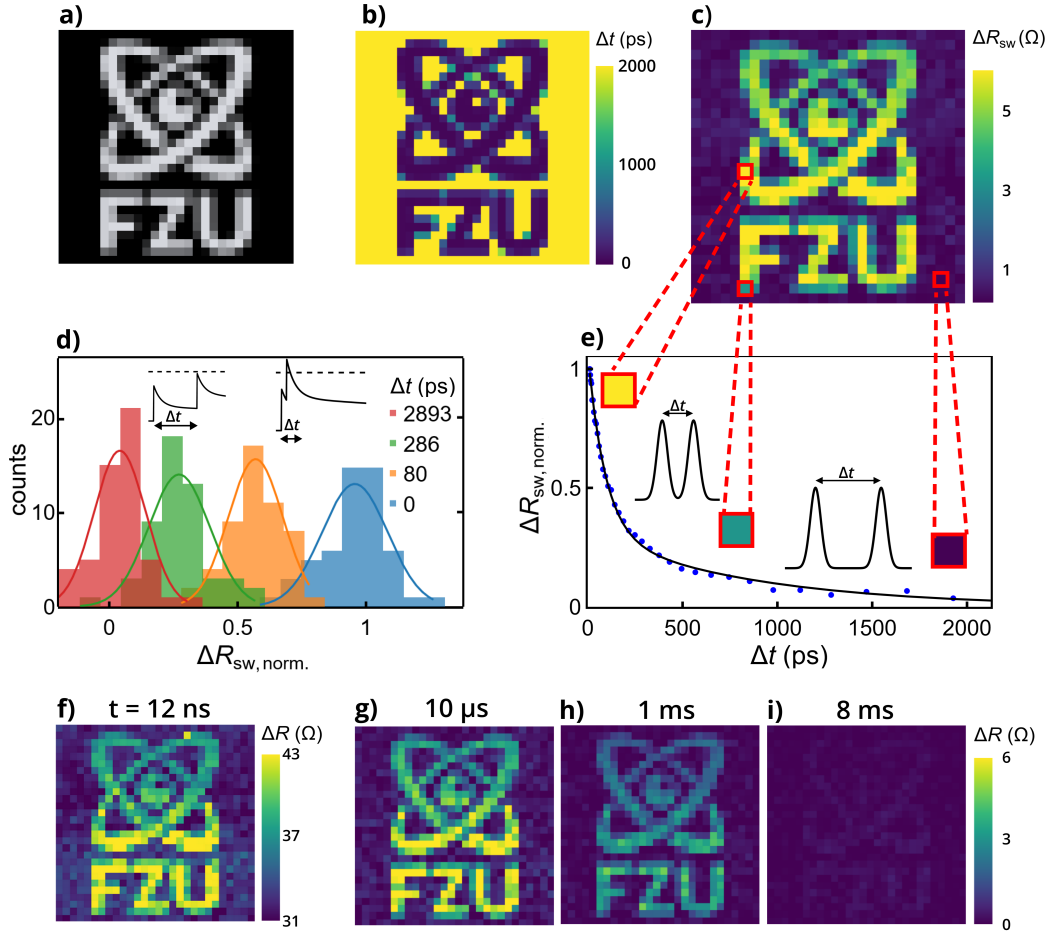


Figure 2: **Temporal latency coding of data from an image.** (a) Original greyscale image with 256 colour levels. (b) Input ns-scale delays. We used a monoexponential fit to the experimental ΔR_{sw} vs. Δt relation to determine the delays, keeping the resulting switching signal ΔR_{sw} linear with the greyscale of the original image. The delays Δt employed ranged from 10 to 2000 ps. (c) Switching signal measured at $10\mu s$ carrying information from the image and correspondence to the experimental ΔR_{sw} vs. Δt dependence (e). The experiment used two laser pulses of equal amplitude and total fluence 33 mJ/cm^2 . The switching signal was normalized to the value for the zero delay. (d) Distributions of switching signal in repeated experiments for selected pulse delays Δt . The plot was created from the data in Fig. 1f using the three curves showing a nonzero signal. (f)-(i) Short- to long-term memory transfer and memory fading demonstrated by resistance readout at different times t after the impact of the pulses. Short-term heat-dominated resistance information (f) is transferred into the long-term switching signal (g), which fades out over a 10-ms period (g-i), after which the memory device can be reused.

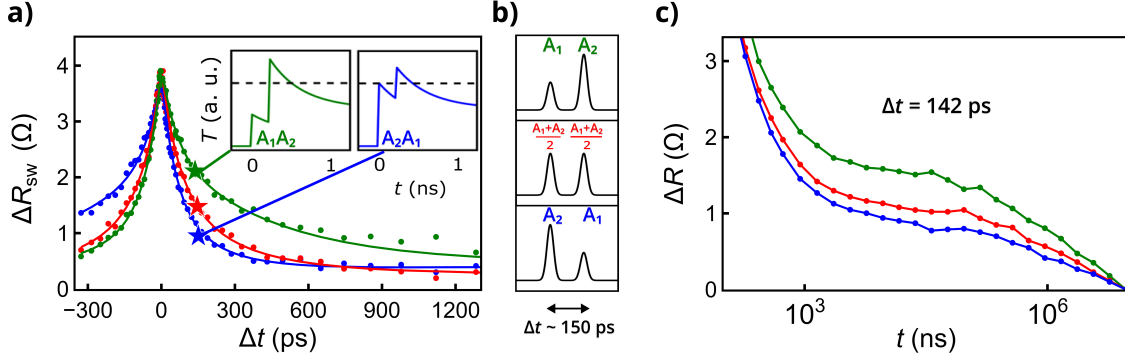


Figure 3: **Recognizing temporal patterns of pulses.** (a) Switching with uneven excitation pulses with the same total energy but different ratios of individual pulse fluences can be used for recognizing pulse patterns at ~ 100 -ps timescales. The inset shows the device's temperature at sub-ns times for sequences of uneven pulses of opposite order A_1A_2 vs. A_2A_1 . Pulses of total commulative fluence $A_1 + A_2 \approx 33$ mJ/cm² with ratios of pulse fluences $\frac{A_1}{A_2} = \frac{2}{1}, \frac{1}{1},$ and $\frac{1}{2}$ were employed as illustrated in (b). (c) Average experimental resistance traces for the three pulse ratios and the delay $\Delta t = 142$ ps.

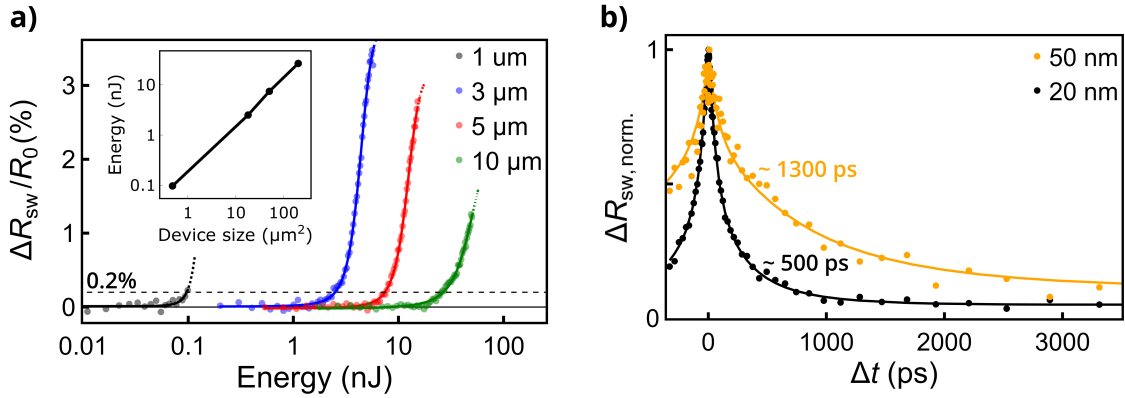


Figure 4: **Scalability and energy efficiency.** (a) Scalability of the devices illustrated by single pulse switching for devices of different nominal widths w prepared from the 20-nm CuMnAs film. For all device sizes, the switching signal dependence on energy adopts the same functional form of a sigmoid. Inset shows the energy of the pulse incident onto the samples' active regions needed to reach the relative switching signal of $\Delta R_{sw}/R_0 = 0.2\%$. The full width at half maximum of the incident Gaussian laser beam was $20 \mu\text{m}$. Nominal dimensions of the active region ($\sim w \times 2w \mu\text{m}^2$) were corrected according to their actual size after preparation by wet etching in the case of the smallest device. For larger devices ($w \gtrsim 3 \mu\text{m}$), these corrections are on the order of $\sim 1\%$ and thus negligible in the presented log-scale. (b) Scaling of device thicknesses leads to different thermal heat dissipation rates as shown by normalized ΔR_{sw} vs. Δt dependence for the 50-nm and 20-nm thick devices with the dimensions of the active region $10 \times 20 \mu\text{m}^2$.

References

- [1] Danijela Marković, Alice Mizrahi, Damien Querlioz, and Julie Grollier. Physics for neuromorphic computing. *Nature Reviews Physics*, 2:499–510, September 2020.
- [2] J. Grollier, D. Querlioz, K. Y. Camsari, K. Everschor-Sitte, S. Fukami, and M. D. Stiles. Neuromorphic spintronics. *Nature Electronics*, 3:360–370, March 2020.
- [3] Jason K. Eshraghian, Max Ward, Emre O. Neftci, Xinxin Wang, Gregor Lenz, Girish Dwivedi, Mohammed Bennamoun, Doo Seok Jeong, and Wei D. Lu. Training Spiking Neural Networks Using Lessons From Deep Learning. *Proceedings of the IEEE*, 111:1016–1054, September 2023.
- [4] Dario Amodei, Danny Hernandez, Girish Sastry, Jack Clark, Greg Brockman, and Ilya Sutskever. Ai and compute, 2018. URL <https://openai.com/research/ai-and-compute>, 4, 2018.
- [5] Or Sharir, Barak Peleg, and Yoav Shoham. The Cost of Training NLP Models: A Concise Overview. Technical report, arXiv, April 2020.
- [6] Pengfei Li, Jianyi Yang, Mohammad A. Islam, and Shaolei Ren. Making AI Less Thirsty: Uncovering and Addressing the Secret Water Footprint of AI Models. Technical report, arXiv, April 2023.
- [7] Dennis Valbjorn Christensen, Regina Dittmann, Bernabe Linares-Barranco, Abu Sebastian, Manuel Le Gallo, Andrea Redaelli, Stefan Slesazeck, Thomas Mikolajick, Sabina Spiga, Stephan Menzel, Ilia Valov, Gianluca Milano, Carlo Ricciardi, Shi-Jun Liang, Feng Miao, Mario Lanza, Tyler J. Quill, Scott Tom Keene, Alberto Salleo, Julie Grollier, Danijela Markovic, Alice Mizrahi, Peng Yao, J. Joshua Yang, Giacomo Indiveri, John Paul Strachan, Suman Datta, Elisa Vianello, Alexandre Valentian, Johannes Feldmann, Xuan Li, Wolfram HP Pernice, Harish Bhaskaran, Steve Furber, Emre Neftci, Franz Scherr, Wolfgang Maass, Srikanth Ramaswamy, Jonathan Tapson, Priyadarshini Panda, Youngeun Kim, Gouhei Tanaka, Simon Thorpe, Chiara Bartolozzi, Thomas A Cleland, Christoph Posch, Shih-Chii Liu, Gabriella Panuccio, Mufti Mahmud, Arnab Neelim Mazumder, Morteza Hosseini, Tinoosh Mohsenin, Elisa Donati, Silvia Tolu, Roberto Galeazzi, Martin Ejsing Christensen, Sune Holm, Daniele Ielmini, and Nini Pryds. 2022 roadmap on neuromorphic computing and engineering. *Neuromorphic Computing and Engineering*, 2(2):022501, May 2022.
- [8] Charlotte Frenkel, David Bol, and Giacomo Indiveri. Bottom-up and top-down approaches for the design of neuromorphic processing systems: Tradeoffs and synergies between natural and artificial intelligence. *Proceedings of the IEEE*, pages 1–30, 2023.
- [9] Yibo Li, Zhongrui Wang, Rivu Midya, Qiangfei Xia, and J. Joshua Yang. Review of memristor devices in neuromorphic computing: materials sciences and device challenges. *Journal of Physics D: Applied Physics*, 51:503002, September 2018.
- [10] Xiubao Sui, Qihao Wu, Jia Liu, Qian Chen, and Guohua Gu. A Review of Optical Neural Networks. *IEEE Access*, 8:70773–70783, 2020.
- [11] Aleksandr Kurenkov, Shunsuke Fukami, and Hideo Ohno. Neuromorphic computing with antiferromagnetic spintronics. *Journal of Applied Physics*, 128:010902, 2020.
- [12] Nathan Leroux, Alice Mizrahi, Danijela Marković, Dédalo Sanz-Hernández, Juan Trastoy, Paolo Bortolotti, Leandro Martins, Alex Jenkins, Ricardo Ferreira, and Julie Grollier. Hardware realization of the multiply and accumulate operation on radio-frequency signals with magnetic tunnel junctions. *Neuromorphic Computing and Engineering*, 1:011001, 2021.

- [13] William A. Borders, Ahmed Z. Pervaiz, Shunsuke Fukami, Kerem Y. Camsari, Hideo Ohno, and Supriyo Datta. Integer factorization using stochastic magnetic tunnel junctions. *Nature*, 573:390–393, September 2019.
- [14] Viola Krizakova, Manu Perumkunnil, Sébastien Couet, Pietro Gambardella, and Kevin Garello. Spin-orbit torque switching of magnetic tunnel junctions for memory applications. *Journal of Magnetism and Magnetic Materials*, 562:169692, 2022.
- [15] Jacob Torrejon, Mathieu Riou, Flavio Abreu Araujo, Sumito Tsunegi, Guru Khalsa, Damien Querlioz, Paolo Bortolotti, Vincent Cros, Kay Yakushiji, Akio Fukushima, Hitoshi Kubota, Shinji Yuasa, Mark D. Stiles, and Julie Grollier. Neuromorphic computing with nanoscale spintronic oscillators. *Nature*, 547:428–431, July 2017.
- [16] Mohammad Zahedinejad, Ahmad A. Awad, Shreyas Muralidhar, Roman Khymyn, Himanshu Fulara, Hamid Mazraati, Mykola Dvornik, and Johan Akerman. Two-dimensional mutually synchronized spin Hall nano-oscillator arrays for neuromorphic computing. *Nature Nanotechnology*, 15:47–52, January 2020.
- [17] Afshin Houshang, Mohammad Zahedinejad, Shreyas Muralidhar, Jakub Checinski, Roman Khymyn, Mona Rajabali, Himanshu Fulara, Ahmad A. Awad, Mykola Dvornik, and Johan Akerman. Phase-Binarized Spin Hall Nano-Oscillator Arrays: Towards Spin Hall Ising Machines. *Physical Review Applied*, 17:014003, January 2022.
- [18] Klaus Raab, Maarten A. Brems, Grischa Beneke, Takaaki Dohi, Jan Rothörl, Fabian Kammerbauer, Johan H. Mentink, and Mathias Kläui. Brownian reservoir computing realized using geometrically confined skyrmion dynamics. *Nature Communications*, 13:6982, November 2022.
- [19] Jakub Zázvorka, Florian Jakobs, Daniel Heinze, Niklas Keil, Sascha Kromin, Samridh Jaiswal, Kai Litzius, Gerhard Jakob, Peter Virnau, Daniele Pinna, Karin Everschor-Sitte, Levente Rózsa, Andreas Donges, Ulrich Nowak, and Mathias Kläui. Thermal skyrmion diffusion used in a reshuffler device. *Nature Nanotechnology*, 14:658–661, July 2019.
- [20] Zufidin Khodzhaev, Emrah Turgut, and Jean Anne C. Incorvia. Analysis of Skyrmion Shuffling Chamber Stochasticity for Neuromorphic Computing Applications. *IEEE Magnetics Letters*, pages 1–5, 2023.
- [21] N. T. Bechler and J. Masell. Helitronics as a potential building block for classical and unconventional computing. *Neuromorphic Computing and Engineering*, 3:034003, 2023.
- [22] Xuan Hu, Can Cui, Samuel Liu, Felipe Garcia-Sanchez, Wesley H. Brigner, Benjamin W. Walker, Alexander J. Edwards, T. Patrick Xiao, Christopher H. Bennett, Naimul Hassan, Michael P. Frank, Jean Anne C. Incorvia, and Joseph S. Friedman. Magnetic skyrmions and domain walls for logical and neuromorphic computing. *Neuromorphic Computing and Engineering*, 3:022003, May 2023.
- [23] Aleksandr Kurenkov, Samik DuttaGupta, Chaoliang Zhang, Shunsuke Fukami, Yoshihiko Horio, and Hideo Ohno. Artificial neuron and synapse realized in an antiferromagnet/ferromagnet heterostructure using dynamics of spin-orbit torque switching. *Advanced Materials*, 0:1900636, 2019.
- [24] H. Bradley, S. Louis, C. Trevillian, L. Quach, E. Bankowski, A. Slavin, and V. Tyberkevych. Artificial neurons based on antiferromagnetic auto-oscillators as a platform for neuromorphic computing. *AIP Advances*, 13:015206, January 2023.
- [25] Jiahao Liu, Teng Xu, Hongmei Feng, Le Zhao, Jianshi Tang, Liang Fang, and Wanjun Jiang. Compensated Ferrimagnet Based Artificial Synapse and Neuron for Ultrafast Neuromorphic Computing. *Advanced Functional Materials*, 32:2107870, 2022.

- [26] Lukas Körber, Christopher Heins, Tobias Hula, Joo-Von Kim, Sonia Thlang, Helmut Schultheiss, Jürgen Fassbender, and Katrin Schultheiss. Pattern recognition in reciprocal space with a magnon-scattering reservoir. *Nature Communications*, 14:3954, July 2023.
- [27] Jack C. Gartside, Kilian D. Stenning, Alex Vanstone, Holly H. Holder, Daan M. Arroo, Troy Dion, Francesco Caravelli, Hidekazu Kurebayashi, and Will R. Branford. Reconfigurable training and reservoir computing in an artificial spin-vortex ice via spin-wave fingerprinting. *Nature Nanotechnology*, 17:460–469, May 2022.
- [28] Kilian D. Stenning, Jack C. Gartside, Luca Manneschi, Christopher T. S. Cheung, Tony Chen, Alex Vanstone, Jake Love, Holly Holder, Francesco Caravelli, Hidekazu Kurebayashi, Karin Everschor-Sitte, Eleni Vasilaki, and Will R. Branford. Neuromorphic overparameterisation and few-shot learning in multilayer physical neural networks. *Nature Communications*, 15:7377, August 2024.
- [29] H. Arava, N. Leo, D. Schildknecht, J. Cui, J. Vijayakumar, P. M. Derlet, A. Kleibert, and L. J. Heyderman. Engineering Relaxation Pathways in Building Blocks of Artificial Spin Ice for Computation. *Physical Review Applied*, 11:054086, May 2019.
- [30] I. T. Vidamour, C. Swindells, G. Venkat, L. Manneschi, P. W. Fry, A. Welbourne, R. M. Rowan-Robinson, D. Backes, F. Maccherozzi, S. S. Dhesi, E. Vasilaki, D. A. Allwood, and T. J. Hayward. Reconfigurable reservoir computing in a magnetic metamaterial. *Communications Physics*, 6:1–11, August 2023.
- [31] William A Borders, Hisanao Akima, Shunsuke Fukami, Satoshi Moriya, Shouta Kurihara, Yoshihiko Horio, Shigeo Sato, and Hideo Ohno. Analogue spin-orbit torque device for artificial-neural-network-based associative memory operation. *Applied Physics Express*, 10:013007, 2016.
- [32] Andrew Ross, Nathan Leroux, Arnaud De Riz, Danijela Marković, Dédalo Sanz-Hernández, Juan Trastoy, Paolo Bortolotti, Damien Querlioz, Leandro Martins, Luana Benetti, Marcel S. Claro, Pedro Anacleto, Alejandro Schulman, Thierry Taris, Jean-Baptiste Begueret, Sylvain Saighi, Alex S. Jenkins, Ricardo Ferreira, Adrien F. Vincent, Frank Alice Mizrahi, and Julie Grollier. Multilayer spintronic neural networks with radiofrequency connections. *Nature Nanotechnology*, 18:1–8, July 2023.
- [33] Miguel Romera, Philippe Talatchian, Sumito Tsunegi, Flavio Abreu Araujo, Vincent Cros, Paolo Bortolotti, Juan Trastoy, Kay Yakushiji, Akio Fukushima, Hitoshi Kubota, Shinji Yuasa, Maxence Ernoult, Damir Vodenicarevic, Tifenn Hirtzlin, Nicolas Locatelli, Damien Querlioz, and Julie Grollier. Vowel recognition with four coupled spin-torque nano-oscillators. *Nature*, 563:230–234, November 2018.
- [34] M. Wang, C. Andrews, S. Reimers, O. J. Amin, P. Wadley, R. P. Champion, S. F. Poole, J. Felton, K. W. Edmonds, B. L. Gallagher, A. W. Rushforth, O. Makarovskiy, K. Gas, M. Sawicki, D. Kriegner, J. Zubáč, K. Olejník, V. Novák, T. Jungwirth, M. Shahrokhvand, U. Zeitler, S. S. Dhesi, and F. Maccherozzi. Spin flop and crystalline anisotropic magnetoresistance in CuMnAs. *Physical Review B*, 101:094429, March 2020.
- [35] Jan Zubáč, Zdeněk Kašpar, Filip Krizek, Tobias Förster, Richard P. Champion, Vít Novák, Tomáš Jungwirth, and Kamil Olejník. Hysteretic effects and magnetotransport of electrically switched cumnas. *Physical Review B*, 104:184424, Nov 2021.
- [36] T. Janda, J. Godinho, T. Ostatnický, E. Pfitzner, G. Ulrich, A. Hoehl, S. Reimers, Z. Šobáň, T. Metzger, H. Reichlová, V. Novák, R. P. Champion, J. Heberle, P. Wadley, K. W. Edmonds, O. J. Amin, J. S. Chauhan, S. S. Dhesi, F. Maccherozzi, R. M. Otxoa, P. E. Roy, K. Olejník, P. Němec, T. Jungwirth, B. Kaestner, and J. Wunderlich. Magneto-seebeck microscopy of domain switching in collinear antiferromagnet cumnas. *Phys. Rev. Materials*, 4:094413, Sep 2020.

- [37] P. Wadley, B. Howells, J. Železný, C. Andrews, V. Hills, R. P. Champion, V. Novák, K. Olejník, F. Maccherozzi, S. S. Dhesi, S. Y. Martin, T. Wagner, J. Wunderlich, F. Freimuth, Y. Mokrousov, J. Kuneš, J. S. Chauhan, M. J. Grzybowski, A. W. Rushforth, K. W. Edmonds, B. L. Gallagher, and T. Jungwirth. Electrical switching of an antiferromagnet. *Science*, 351:587–590, February 2016.
- [38] Kamil Olejník, Tom Seifert, Zdeněk Kašpar, Vít Novák, Peter Wadley, Richard P. Champion, Manuel Baumgartner, Pietro Gambardella, Petr Němec, Joerg Wunderlich, et al. Terahertz electrical writing speed in an antiferromagnetic memory. *Science advances*, 4:eaar3566, 2018.
- [39] Peter Wadley, Sonka Reimers, Michal J. Grzybowski, Carl Andrews, Mu Wang, Jasbinder S. Chauhan, Bryan L. Gallagher, Richard P. Champion, Kevin W. Edmonds, Sarnjeet S. Dhesi, Francesco Maccherozzi, Vít Novák, Joerg Wunderlich, and Tomas Jungwirth. Current polarity-dependent manipulation of antiferromagnetic domains. *Nature Nanotechnology*, 13:362–365, 2018.
- [40] O. J. Amin, S. F. Poole, S. Reimers, L. X. Barton, A. Dal Din, F. Maccherozzi, S. S. Dhesi, V. Novák, F. Krizek, J. S. Chauhan, R. P. Champion, A. W. Rushforth, T. Jungwirth, O. A. Tretiakov, K. W. Edmonds, and P. Wadley. Antiferromagnetic half-skyrmions electrically generated and controlled at room temperature. *Nature Nanotechnology*, 18:1–5, May 2023.
- [41] Z. Kašpar, M. Surýnek, J. Zubáč, F. Krizek, V. Novák, R. P. Champion, M. S. Wörnle, P. Gambardella, X. Marti, P. Němec, K. W. Edmonds, S. Reimers, O. J. Amin, F. Maccherozzi, S. S. Dhesi, P. Wadley, J. Wunderlich, K. Olejník, and T. Jungwirth. Quenching of an antiferromagnet into high resistivity states using electrical or ultrashort optical pulses. *Nature Electronics*, 4:30–37, Nov 2020.
- [42] Sonka Reimers, Dominik Kriegner, Olena Gomonay, Dina Carbone, Filip Krizek, Vít Novák, Richard P. Champion, Francesco Maccherozzi, Alexander Björling, Oliver J. Amin, Luke X. Barton, Stuart F. Poole, Khalid A. Omari, Jan Michalička, Ondřej Man, Jairo Sinova, Tomáš Jungwirth, Peter Wadley, Sarnjeet S. Dhesi, and Kevin W. Edmonds. Defect-driven antiferromagnetic domain walls in CuMnAs films. *Nature Communications*, 13:724, February 2022.
- [43] O. J. Amin, S. Reimers, F. Maccherozzi, S. S. Dhesi, V. Novák, R. P. Champion, K. W. Edmonds, and P. Wadley. Electrical control of 180° domain walls in an antiferromagnet. *APL Materials*, 11:091112, September 2023.
- [44] Filip Krizek, Sonka Reimers, Zdeněk Kašpar, Alberto Marmodoro, Jan Michalička, Ondřej Man, Alexander Edström, Oliver J. Amin, Kevin W. Edmonds, Richard P. Champion, Francesco Maccherozzi, Samjeet S. Dhesi, Jan Zubáč, Dominik Kriegner, Dina Carbone, Jakub Železný, Karel Výborný, Kamil Olejník, Vít Novák, Jan Rusz, Juan-Carlos Idrobo, Peter Wadley, and Tomas Jungwirth. Atomically sharp domain walls in an antiferromagnet. *Science Advances*, 8:eabn3535, March 2022.
- [45] M. Surýnek, V. Saidl, Z. Kašpar, V. Novák, R. P. Champion, P. Wadley, and P. Němec. Investigation of magnetic anisotropy and heat dissipation in thin films of compensated antiferromagnet CuMnAs by pump–probe experiment. *Journal of Applied Physics*, 127:233904, June 2020.
- [46] M. Surýnek, J. Zubac, K. Olejnik, A. Farkas, F. Krizek, L. Nadvornik, P. Kubascik, F. Trojanek, R. P. Champion, V. Novak, T. Jungwirth, and P. Nemeec. Picosecond transfer from short-term to long-term memory in analog antiferromagnetic memory device. *arXiv preprint arXiv:2401.17370*, 2024.
- [47] Ramesh Singh, Radhika Sukapuram, and Suchetana Chakraborty. A survey of mobility-aware Multi-access Edge Computing: Challenges, use cases and future directions [Download:

<https://authors.elsevier.com/a/1gA9O5bBBBSxhr>. *Ad Hoc Networks*, 140:103044, November 2022.

- [48] Anson Ho, Ege Erdil, and Tamay Besiroglu. Limits to the Energy Efficiency of CMOS Microprocessors. Technical report, December 2023.
- [49] Michelle Wijshoff, Robert Carpenter, Giacomo Talmelli, Sebastien Couet, Claudia Fleischmann, and Kristiaan Temst. Enhanced SOT Efficiency in Pt/Co Systems with a NiO Interlayer for SOT-MRAM. In *2024 IEEE International Magnetic Conference - Short papers (INTERMAG Short papers)*, pages 1–2, May 2024.
- [50] Siddharth Rao, Kaiming Cai, Giacomo Talmelli, Nathali Franchina-Vergel, Ward Janssens, Hubert Hody, Farrukh Yasin, Kurt Wostyn, and Sebastien Couet. Spin-orbit torque MRAM for ultrafast cache and neuromorphic computing applications. In *2023 IEEE International Memory Workshop (IMW)*, pages 1–4, May 2023.
- [51] Yeongjun Lee, Hea-Lim Park, Yeongin Kim, and Tae-Woo Lee. Organic electronic synapses with low energy consumption. *Joule*, 5:794–810, April 2021.
- [52] Yoeri van de Burgt, Ewout Lubberman, Elliot J. Fuller, Scott T. Keene, Grégorio C. Faria, Sapan Agarwal, Matthew J. Marinella, A. Alec Talin, and Alberto Salleo. A non-volatile organic electrochemical device as a low-voltage artificial synapse for neuromorphic computing. *Nature Materials*, 16:414–418, April 2017.
- [53] Joshua Robertson, Matěj Hejda, Julián Bueno, and Antonio Hurtado. Ultrafast optical integration and pattern classification for neuromorphic photonics based on spiking VCSEL neurons. *Scientific Reports*, 10:6098, April 2020.
- [54] K Olejník, Z Kašpar, J Zubáč, S Telkamp, A Farkaš, Kriegner D, Výborný K, J Železný, Z Šobáň, P Zheng, T Jungwirth, , V Novák, and F Krizek. Quench switching of mn₂as. 2024. in preparation.
- [55] Filip Krizek, Zdeněk Kašpar, Aliaksei Vetushka, Dominik Kriegner, Elisabetta M. Fiordaliso, Jan Michalicka, Ondřej Man, Jan Zubáč, Martin Brajer, Victoria A. Hills, Kevin W. Edmonds, Peter Wadley, Richard P. Champion, Kamil Olejník, Tomáš Jungwirth, and Vít Novák. Molecular beam epitaxy of CuMnAs. *Physical Review Materials*, 4:014409, January 2020.

Neuromorphic information processing using ultrafast heat dynamics and quench switching of an antiferromagnet: Supplementary material

J. Zubáč^{*†1,2}, M. Surýnek^{†2}, K. Olejník¹, A. Farkaš^{1,2}, F. Krizek¹, L. Nádvorník², P. Kubaščík², Z. Kašpar^{1,2}, F. Trojánek², R. P. Campion³, V. Novák¹, P. Němec², and T. Jungwirth^{1,3}

¹Institute of Physics of the Czech Academy of Sciences, Prague, Czech Republic

²Faculty of Mathematics and Physics, Charles University, Prague, Czech Republic

³School of Physics and Astronomy, University of Nottingham, United Kingdom

1 Schematics of a neuron and neuromorphic functionalities

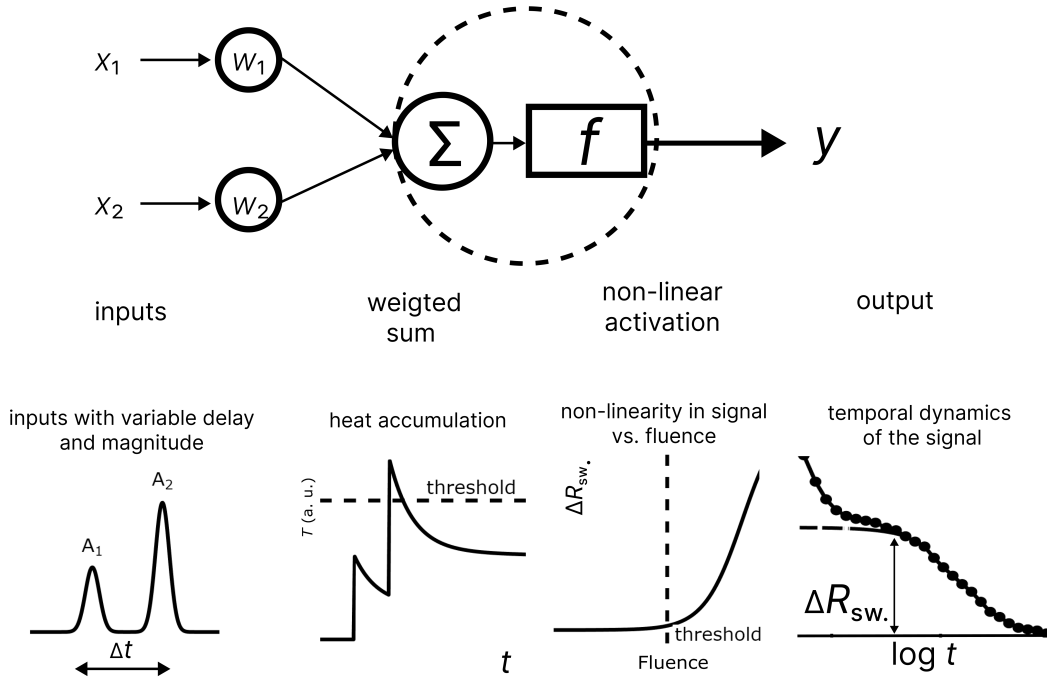


Figure S1: **Schematics of a neuron and neuromorphic functionalities.** An artificial neuron takes two inputs, performs their weighted summation and passes the result through a non-linear activation function. Analogous functionalities in the antiferromagnetic memory device: Two excitation laser pulses with variable delays and magnitudes heat the sample. Once the temperature threshold is reached, switching signal $\Delta R_{sw.}$ is observed. Twofold dynamics - short-term heat dynamics and long-term switching dynamics characterize the behaviour of the sample.

*Email: zubac@fzu.cz

†These authors contributed equally.

2 Heat dissipation model for two unequal pulses

To explain the observed behaviour from Fig. 3 used for the recognizing temporal patterns of pulses, we extend the previously presented heat dissipation model using two pulses of the same magnitude from Ref. [1] into a case when the excitation laser pulses are unequal. The dissipation of laser-induced heat into a metallic sample at picosecond times is usually described by a phenomenological two-temperature model considering electron and phonon subsystems of a sample with different temperatures. Following the absorption of laser pulse energy by the electron subsystem and subsequent electron thermalization, the phonon and electron subsystem's temperatures equalize with a characteristic time constant ~ 2.4 ps [2]. At longer times, the thermal relaxation mediated by phonons with ~ 100 -ps dynamics dominates the heat dissipation process, followed by the heat diffusion from the substrate to other thermally connected parts of the experimental setup (sample holder, etc.) with an observed characteristic time constant $\tau_{\text{subst}} \sim 10$ ns. In the case of a single pulse hitting the sample at the time $t = 0$, this process can be described by a function

$$f(t) = (A - B) \exp\left(-\frac{t}{\tau_{\text{ph}}}\right) + B \exp\left(-\frac{t}{\tau_{\text{subst}}}\right), \quad (\text{S1})$$

where τ_{ph} and τ_{subst} are the time constants, A is the amplitude of the laser pulse, $A - B$ represents a portion of heat dissipated with the dynamics given by the τ_{ph} and B is the heat contributing to overall heating of the substrate. Assuming the maximal temperature change is approximately proportional to the absorbed laser fluence, the function $f(t)$ can be interpreted as the sample's temperature change. Considering two laser pulses, the first impacting the sample at time $t = 0$ and the second at $t = \Delta t$, the temperature's time evolution can be roughly approximated as

$$\Delta T_{12}(t) = f_1(t) + f_2(t - \Delta t) \approx A_1 \exp^+\left(-\frac{t}{\tau_{\text{ph}}}\right) + A_2 \exp^+\left(-\frac{t - \Delta t}{\tau_{\text{ph}}}\right), \quad (\text{S2})$$

where $\exp^+(-x) = \exp(-x)\Theta(x)$ is the exponential function multiplied by the Heaviside step function $\Theta(x)$.

In Fig. S2, we simulate the sample temperature using equations Eq. S1 and Eq. S2 during the double pulse experiment and illustrate the resulting switching signal. Fig. S2a shows the temperature change for two pulses of the same pulse magnitude but opposite order as a function of laboratory time, t . Since the amplitudes A_1 and A_2 in Eq. S2 are weighted by exponential dissipation factors shifted in time, the heating by two pulses in times $t \lesssim \tau_{\text{th}}$ does not correspond to a combined effect as if the pulse fluences were summed, but leads to a higher maximal temperature when the smaller pulse is followed by a larger than in the opposite case. In Fig. S2b, we plot the corresponding dependence of maximum reached temperature on the pulse delay, Δt , for different fluence ratios but the same sum of pulse fluences. The parameters used were the same as in Fig. S2a; we added the reference curve for $A_1 = A_2$. The depicted curves increase with decreasing delay and reach the same value in the overlap ($\Delta t = 0$). For a non-zero delay, the curve splits into three branches for $A_1 > A_2$, $A_1 = A_2$ and $A_1 < A_2$. To obtain the switching signal, we assumed the sigmoidal relation between ΔR and the maximal reached temperature, T_{max} :

$$\Delta R = \frac{A_S}{1 + \exp\left(-\frac{T_{\text{max}} - T_C}{K}\right)} \quad (\text{S3})$$

where A_S is the sigmoid amplitude, K is parameter characterizing its width and T_C sigmoid's center. The sigmoid function provides a good fit for the experimental data (see inset of Fig. 1f) and represents the nonlinear activation function widely used in machine learning and neural networks.

Fig. S2d shows the resulting switching signal as a function of the pulse delay obtained by applying the sigmoidal function to the dependences in Fig. S2b. The splitting of the switching signal into three separate branches for non-zero Δt and different pulse amplitude ratios here is thus the consequence of the different maximal temperatures reached. Due to the application of non-linear sigmoid, the dependence of ΔR on Δt is steeper than the T_{max} vs Δt dependence. From an experimental viewpoint, the difference between T vs Δt and the ΔR vs Δt dependence is also

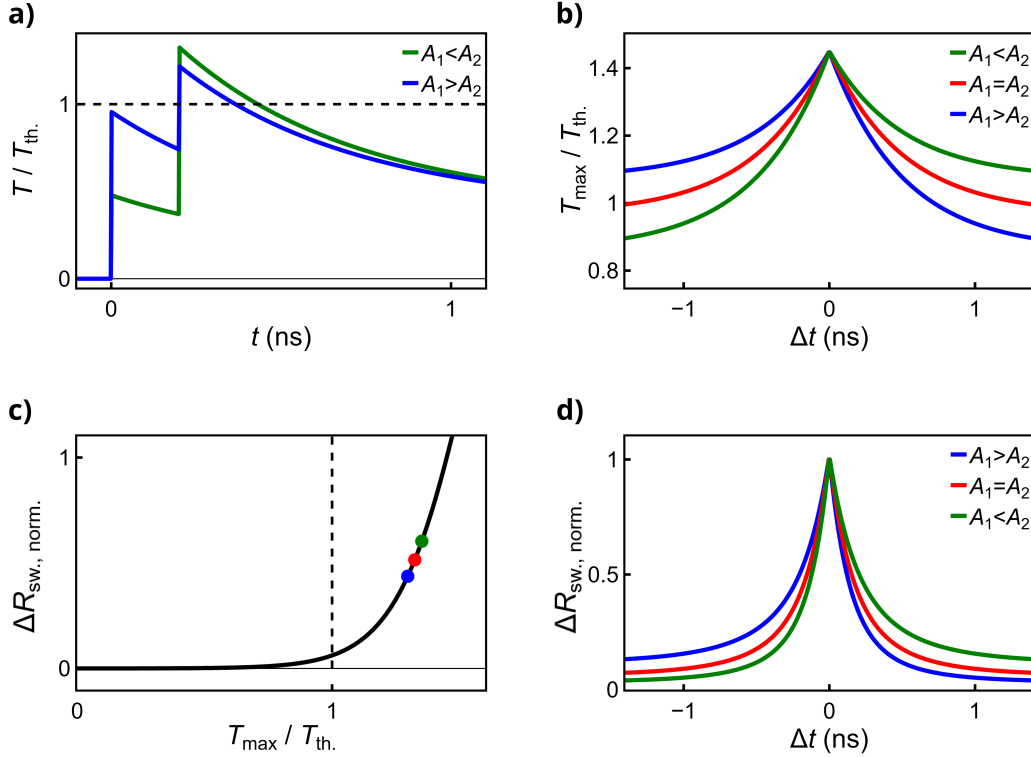


Figure S2: **Calculated sample temperature after the impact of two laser pulses of various fluence amplitude ratios and the corresponding switching signal.** Dissipation rates $\tau_{\text{ph}} = 0.5$ ns and $\tau_{\text{subst}} = 10$ ns, and amplitudes $A_1 + A_2 = 1.45 F_{\text{th}}$ were used. The ratio of pulse amplitudes is $\frac{A_1}{A_2} = \frac{1}{2}$ for $A_1 < A_2$ and $\frac{A_1}{A_2} = \frac{2}{1}$ for $A_1 > A_2$. Parameters of the sigmoid were obtained from the fit to experimental data (inset of Fig. 1f). **(a)** Temporal dependence of the sample temperature after the impact of two pulses with the same fluences but opposite order and the delay $\Delta t = 150$ ps. **(b)** Delay dependence of the sample temperature for the three pulse ratios. **(c)** Nonlinear sigmoidal dependence of the switching signal on the maximal temperature. The signal value was normalized to the value reached in the pulse overlap. The coloured dots represent the signal values for the three amplitude ratios depicted in **(b)** and the pulse delay $\Delta t = 150$ ps. **(d)** The resulting switching signal as a function of pulse delay.

the in the detection: Whereas the temperature is subject of ultrafast dynamics and appropriate method has to be chosen for the fast and precise sub-ns detection, the switching signal ΔR is governed by millisecond dynamics and can be recorded by a conventional electrical readout much later after the pulse impact. This way, we can obtain the information about the temperature through ΔR . For the given Δt and non-equal pulse amplitudes A_1 and A_2 , it means we can determine their order thanks to the different resulting signal ΔR .

3 Applications using two unequal pulses

3.1 Recognition of pulse patterns based on experimental data

To determine pulse patterns of two pulses at sub-ns times from noisy experimental data (Fig. S3a), we performed the classification into four classes corresponding to the four possible combinations of pulses with amplitudes A_1 and A_2 using the support vector machine classifier SVC from Python scikit-learn package [3]. The input dataset consisted of 192 class-balanced resistance traces with 100 log-spaced data points complemented by the size of the switching signal for each of the traces.

We splitted the dataset equally into train and test subsets and performed the supervised machine learning on the train data. To find a proper SVC classifier model and its hyperparameters, we employed the GridSearchCV routine from the scikit-learn package, examining 1200 models in total with various support vector machine kernels ('linear', 'poly', 'rbf' or 'sigmoid') and values of a regularizing parameter C . The best result, which lead to test accuracy of 97.9%, was obtained for the polynomial kernel of fourth degree, and the value of $C = 0.001149$. Reducing the dataset traces to data points ranging from 200 ns to 10 ms where the switching signal dominates the resistance variation and repeating the same procedure lead to somewhat lower accuracy of 86%.

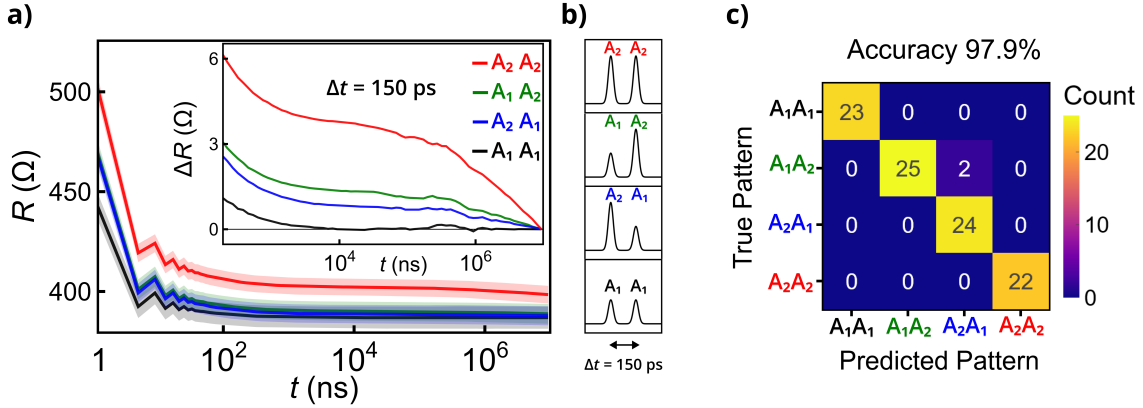


Figure S3: **Recognition of temporal pulse patterns using resistance readout.** (a) Experimental resistance data in the 10-ms range for all four combinations of pulse amplitudes $A_1 = 11.15$ mJ/cm² and $A_2 = 22.30$ mJ/cm² (pictured in (b)) and pulse delay $\Delta t = 150$ ps. For each of the four combinations, the dataset includes 48 resistance traces represented by their mean value (thick line) and standard deviation (shaded region corresponds to $\pm 0.5 \sigma$), totalling 192 traces. The inset shows the detail of ΔR from 200 ns to 10 ms. (c) Results of the pulse pattern recognition with the test accuracy of 97.9 % displayed as a confusion matrix. Further details in the text.

3.2 Convolutional edge detection

Next, in Fig. S4, we propose the application of unequal pulse-pattern recognition for convolutional edge detection. We conveniently map the binary image pixel values onto the fluences of the two pulses. The pulses, delayed by ~ 150 ps, are then used as the experimental inputs - pulse amplitudes. The image is processed sequentially, similarly as in the case of Fig. 2. The detected edge corresponds to the situation when the stronger pulse follows the weaker and the switching signal exceeds a switching threshold R_{th} : $\Delta R_{sw, A_1 < A_2} < R_{th} < \Delta R_{sw, A_1 > A_2}$.

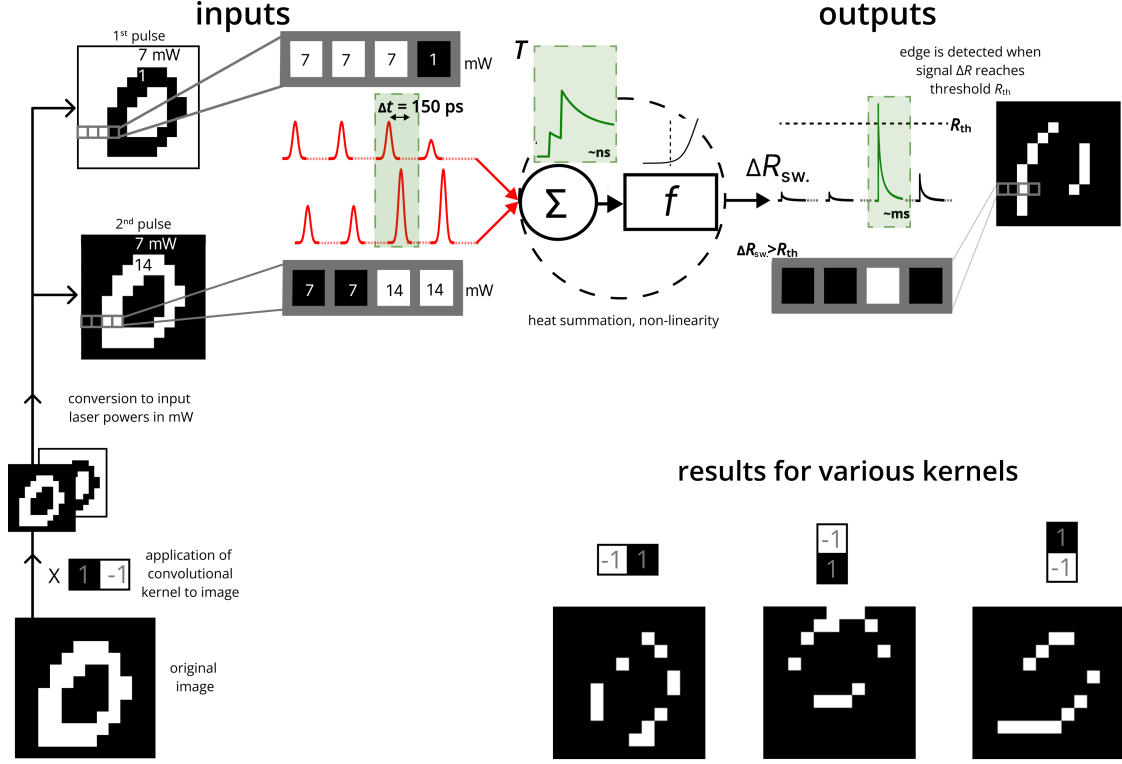


Figure S4: **Recognizing patterns of pulses used for convolutional edge detection.** Application of the 2×1 convolutional kernel to the original binary image leads to a Hadamard product of the size twice as large as the original image which corresponds to the copy of the original image and its inverse shifted by one pixel. The binary values of the image are converted to the laser fluences for the individual pulses and shined pulse by pulse to the sample with a fixed delay of $\Delta t = 150$ ps. This leads accumulation of heat at ns-scale which determines the resistance signal ΔR measured at ms-scale. The edge is detected only when the resistance signal ΔR exceeds a certain limit which corresponds to the situation when the 7 mW pulse is followed by the 14 mW. Below are displayed results of the convolutional edge detection for various kernels.

4 Experimental setup

The schematics of the experimental setup consisting of the optical part used for excitation of the sample and the electrical part for resistance readout is depicted in Fig. S5.

4.1 Electrical measurements

Time-resolved electrical measurements were performed using Rohde & Schwarz RTP064 high-performance oscilloscope with 6 GHz bandwidth for readout and Rigol DG1000Z as a voltage source. We recorded the voltage U of the input resistance of the oscilloscope connected in series with the sample. The sample's resistance was then obtained from $R = \frac{U_{\text{source}} * R_{\text{scope}}}{U} - R_{\text{scope}}$ by reducing R with the oscilloscope attenuation factor: $R_{\text{sample}} = R / \sqrt{10^{\text{atten}[\text{dB}]/10}}$. We typically collected 2.5M points over a 10 μs or a 10 ms window during one acquisition, which was started by receiving a timing reference signal from the laser. To reduce the noise at high frequencies without losing the time resolution, we acquired the data in a stroboscopic regime with a 100-Hz laser duty cycle and averaged out curves from ~ 100 acquisitions.

4.2 Optical measurements

Fig. S4 shows the experimental setup consisting of the electrical readout and optical part, enabling the sample's excitation by a pair of time-delayed laser pulses. The optical part of the setup involves femtosecond laser system Pharos by Light Conversion delivering pulses with duration of 150 fs and wavelength of 1030 nm, and the delay line (DL) allowing for adjusting the mutual delay of laser pulses (Δt) in the interval from -0.5 to 4 ns. Further details about the experimental setup can be found in Ref. [1].

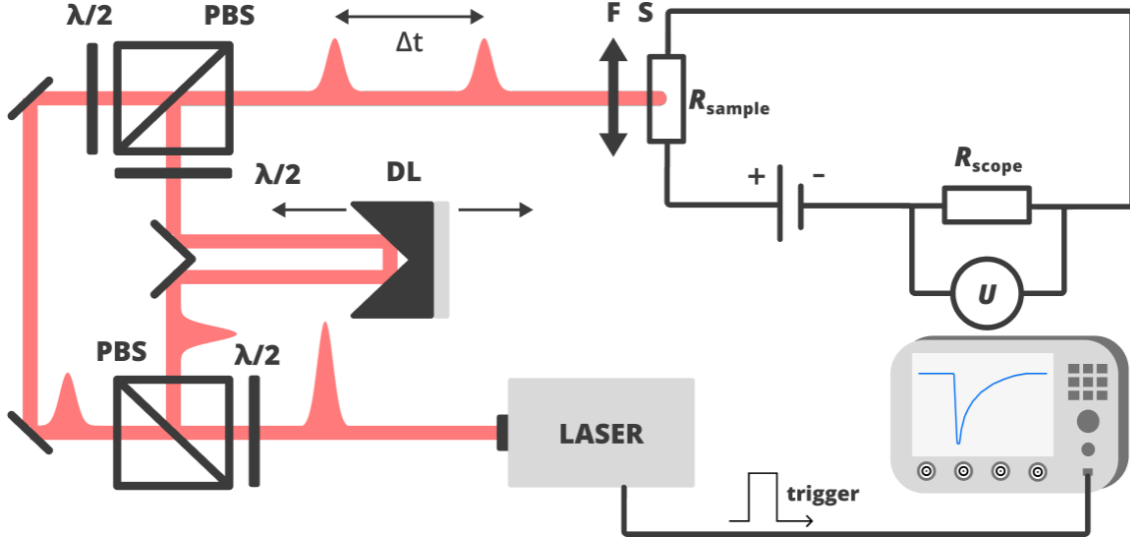


Figure S5: Experimental setup - optical (left) and electrical (right) part.

4.3 Comparison of electrical and optical readout

Fig. S6 was obtained using the experimental setup shown in Fig. S5. In addition to electrical readout, differential optical reflectivity was measured using an avalanche photodiode in a pump-probe configuration. Sub-threshold laser pulses probed the sample at a frequency of 1000 Hz, while the pump pulses were pulse-picked by a factor of 10, delivering optical excitation every 10 ms. The time delay between pump and probe pulses was fixed at $\Delta t = 100$ ps. By comparing the electrical readout (Fig. S6a) with the optical reflectivity (Fig. S6b) during the 10 ms writing time window, we correlated the onset of CuMnAs switching in the sample's resistance with changes in reflectivity when excited with over-threshold pump pulses.

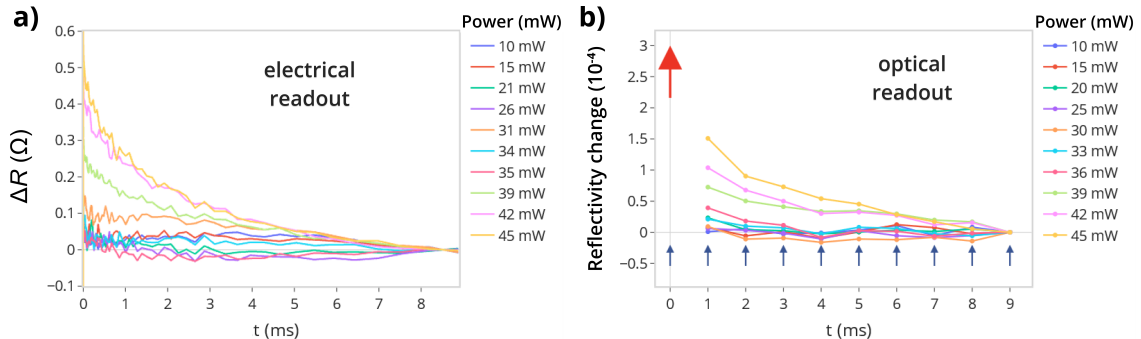


Figure S6: Comparison of electrical resistance readout (a) and the optical reflectivity readout (b) for several different laser powers.

References

- [1] M Surynek, J Zubac, K Olejnik, A Farkas, F Krizek, L Nadvornik, P Kubascik, F Trojanek, RP Champion, V Novak, T Jungwirth, and P Nemeč. Picosecond transfer from short-term to long-term memory in analog antiferromagnetic memory device. *arXiv preprint arXiv:2401.17370*, 2024.
- [2] M. Surýnek, V. Saidl, Z. Kašpar, V. Novák, R. P. Champion, P. Wadley, and P. Němec. Investigation of magnetic anisotropy and heat dissipation in thin films of compensated antiferromagnet CuMnAs by pump–probe experiment. *Journal of Applied Physics*, 127:233904, June 2020.
- [3] Fabian Pedregosa, Gaël Varoquaux, Alexandre Gramfort, Vincent Michel, Bertrand Thirion, Olivier Grisel, Mathieu Blondel, Peter Prettenhofer, Ron Weiss, Vincent Dubourg, et al. Scikit-learn: Machine learning in python. *the Journal of machine Learning research*, 12:2825–2830, 2011.